Liquid Rope Coiling

Neil M. Ribe,[1] Mehdi Habibi,[2] and Daniel Bonn[3]

[1]Lab FAST, Université Pierre et Marie Curie, Université Paris-Sud, CNRS, 91405 Orsay, France; email: ribe@fast.u-psud.fr

[2]Department of Physics, Institute for Advanced Studies in Basic Sciences (IASBS), Zanjan 45195-1159, Iran; email: habibi@iasbs.ac.ir

[3]Laboratoire de Physique Statistique, Ecole Normale Supérieure, 75005 Paris, France, and Van der Waals–Zeeman Institute, Institute of Physics, University of Amsterdam, 1090 GL Amsterdam, The Netherlands; email: bonn@lps.ens.fr

Annu. Rev. Fluid Mech. 2012. 44:249–66

First published online as a Review in Advance on October 10, 2011

The *Annual Review of Fluid Mechanics* is online at fluid.annualreviews.org

This article's doi: 10.1146/annurev-fluid-120710-101244

0066-4189/12/0115-0249$20.00

Keywords

buckling instabilities, spiral waves, supercoiling, non-Newtonian fluids, Kaye effect, fluid-mechanical sewing machine

Abstract

A thin stream or rope of viscous fluid falling from a sufficient height onto a surface forms a steadily rotating helical coil. Tabletop laboratory experiments in combination with a numerical model for slender liquid ropes reveal that finite-amplitude coiling can occur in four distinct regimes (viscous, gravitational, inertio-gravitational, and inertial) corresponding to different balances among the three principal forces acting on the rope. The model further shows that the onset of coiling has distinct viscous, gravitational, and inertial modes that connect smoothly with the corresponding finite-amplitude regimes. In addition to steady coiling, slender liquid ropes falling onto surfaces can exhibit a remarkable variety of nonstationary behaviors, including propagating spiral waves of air bubbles, supercoiling, the leaping-shampoo (Kaye) effect for non-Newtonian fluids, and the fluid-mechanical sewing machine in which the rope leaves complex stitch patterns on a moving surface.

1. INTRODUCTION

Rope: in the context of this review, a slender body with significant resistance to deformation by bending

Buckling instability: the onset of deformation by bending in a slender (or thin) object subject to an axial (or lateral) compressive stress

Slender body: a body with two characteristic dimensions (radius or thickness) much smaller than the third

Perhaps the simplest experiment in all of fluid mechanics is to pour a very thin stream of viscous fluid such as honey onto a surface from a height of approximately 10 cm. Rather than approaching the surface vertically as one might expect, the fluid stream builds a beautiful helical structure that resembles a pile of coiled rope (**Figure 1*a***). This characteristic appearance led Barnes & Woodcock (1958) to call the phenomenon the "liquid rope coil" effect.

The origin of liquid rope coiling is a buckling instability in which an initially vertical fluid stream subject to an axial compressive stress becomes unstable to deformation by bending. As such, liquid rope coiling belongs to a wider class of buckling instabilities of thin and/or slender objects that include rods, filaments, ribbons, and sheets of material whose rheology may be anything from purely viscous to purely elastic. A few particularly striking examples are shown in **Figure 1*b–e***.

Yet among the countless examples of buckling instabilities in nature and technology, liquid rope coiling holds a special place for several reasons. First, clean and accurate laboratory experiments are easy to perform without complications from undesirable symmetry-breaking features of the apparatus (e.g., the finite length of extrusion slots that prevents truly two-dimensional experiments on the folding of viscous sheets). Second, coiling is a steady-state phenomenon when observed from within the corotating reference frame that follows the steady circular motion of the contact point of the liquid rope with the surface onto which it falls. This permits liquid rope coiling to be investigated with the help of powerful analytical and numerical tools that are much more difficult to apply to inherently time-dependent buckling instabilities such as the periodic folding of sheets. Finally, and on a more personal note, we find that coiling possesses a particular beauty and elegance that it shares with the many other spiral and helical forms found in the natural world.

2. MATHEMATICAL DESCRIPTION OF SLENDER LIQUID ROPES

Before setting out, we have to decide what to call the objects under study. In the theory of elasticity, a distinction is commonly made between slender rods, which resist deformation by

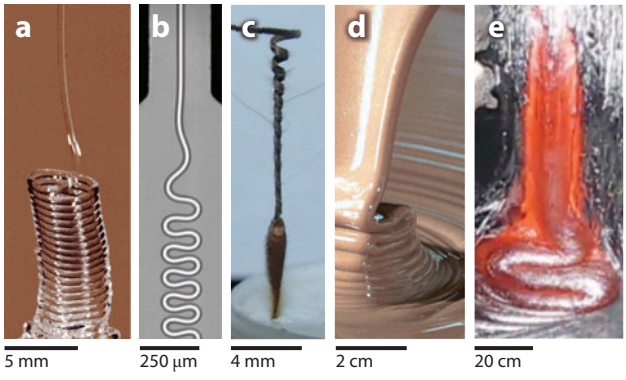

Figure 1

Examples of buckling instabilities. (*a*) Coiling of silicone oil with viscosity $\nu = 10^5$ cSt. Photograph taken from Mahadevan et al. (1998), reproduced with permission from Nature Publishing Group. (*b*) Folding of a rope of silicone oil ($\nu = 10^4$ cSt) in a microchannel filled with silicone oil with $\nu = 5$ cSt. Photograph courtesy of T. Cubaud. (*c*) Desiccation-induced coiling of the self-burying seed of *Erodium cicutarium*. (*d*) Periodic folding of a falling sheet of molten chocolate. Photograph courtesy of Mars Inc. (*e*) Periodic folding of a falling lava stream (see the Related Resources section for a link to a video). Photograph from the U.S. Geological Survey.

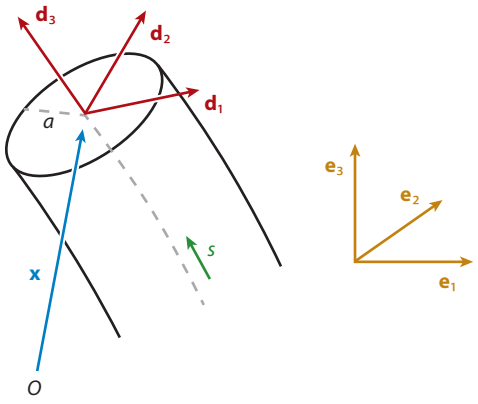

Figure 2

Geometry of a slender viscous rope. Figure modified from Ribe (2004).

bending, and strings, which do not (Landau & Lifshitz 1986). However, because the term rod seems inappropriate for a fluid, we use the terms rope and string for slender fluid bodies with and without resistance to bending, respectively.

A viscous rope is slender if its radius a is small relative to its length and to the local radius of curvature of its axis. Such objects are amenable to a simplified description in which the full three-dimensional Navier-Stokes equations are reduced to equivalent one-dimensional equations that involve only variables defined along the rope's central axis (Arne et al. 2010, Eggers & Dupont 1994, Entov & Yarin 1984, Ribe et al. 2006a, Yarin 1993). The description divides naturally into geometrical, kinematical, and dynamical aspects. Because surface tension has a relatively minor (1%–20%) effect on the coiling frequency for typical experimental fluids, we neglect it in the following discussion, although it is easy to include in the equations if desired (Eggers & Dupont 1994, Ribe et al. 2006a).

Figure 2 shows a portion of a slender liquid rope. The rope's geometry is described by the Cartesian coordinates $\mathbf{x}(s, t)$ of its axis and its radius $a(s, t)$, where s is the arc length along the axis and t is time. Given $\mathbf{x}(s, t)$, the unit vector tangent to the axis is

$$\mathbf{d}_3(s, t) = \mathbf{x}', \tag{1}$$

where the prime denotes $\partial/\partial s$. At each point along the axis, we define orthogonal unit vectors $\mathbf{d}_1(s, t)$ and $\mathbf{d}_2(s, t) \equiv \mathbf{d}_3 \times \mathbf{d}_1$ in the plane of the rope's cross section. Although the orientation of $\mathbf{d}_1$ and $\mathbf{d}_2$ at each point along the axis can be chosen arbitrarily, it is convenient in practice to define them to be material unit vectors that follow the rotation of the fluid about the axis. The rates of change of the basis vectors $\mathbf{d}_i$ along the axis are given by the generalized Frenet relations

$$\mathbf{d}'_i = \boldsymbol{\kappa} \times \mathbf{d}_i, \tag{2}$$

where $\boldsymbol{\kappa} \equiv \kappa_i \mathbf{d}_i$ is the curvature vector. The curvatures κ_i can be expressed in terms of arcwise derivatives of the three Eulerian angles [or, more conveniently for numerical purposes, the four Euler parameters (Whittaker 1944)] that describe the orientation of the basis $\mathbf{d}_i$ relative to a fixed external basis $\mathbf{e}_i$.

String: a slender body with negligible resistance to deformation by bending

Turning now to kinematics, we introduce the velocity $\mathbf{V} \equiv V_i \mathbf{d}_i$ of the fluid on the axis. Because the rope is slender, points that are located instantaneously on the (geometrically defined) axis are material points to an excellent approximation. The velocity $\mathbf{V}$ is therefore related to the

coordinates **x** by

$$\frac{D\mathbf{x}}{Dt} = \mathbf{V}, \tag{3}$$

Bending/twisting moment vector: the first moment of the vector force acting on a cross section of a slender body (Equation 7)

where D/Dt is a material derivative that follows the stretching of the rope (Buckmaster et al. 1975).

Given the velocity field $\mathbf{V}(s, t)$ on the axis, the next step is to write down expressions for the rates of strain and rotation that are required to describe the deformation of the rope by stretching, bending, and twisting. The rate of stretching of the rope's axis is

$$\Delta = \mathbf{V}' \cdot \mathbf{d}_3. \tag{4}$$

Moreover, because the rate of thinning of the rope is directly proportional to the rate at which its axis is stretched, conservation of mass requires

$$\frac{DA}{Dt} = -A\Delta, \tag{5}$$

where $A \equiv \pi a^2$ is the area of a cross section. Next, the rates of rotation of the axis about the directions $\mathbf{d}_1$ and $\mathbf{d}_2$, respectively, are

$$\omega_1 = -\mathbf{V}' \cdot \mathbf{d}_2, \quad \omega_2 = \mathbf{V}' \cdot \mathbf{d}_1. \tag{6}$$

Finally, the spin ω_3 of the fluid about the direction $\mathbf{d}_3$ is a primitive variable with no intrinsic relation to the components of **V**.

The fundamental quantities required to describe the rope's dynamics are the force $\mathbf{N}(s, t)$ acting on a cross section and the vector $\mathbf{M}(s, t)$ of bending and twisting moments, defined as

$$\mathbf{N} \equiv N_i \mathbf{d}_i = \int \boldsymbol{\sigma} \cdot \mathbf{d}_3 \, dA, \quad \mathbf{M} \equiv M_i \mathbf{d}_i = \int \mathbf{y} \times (\boldsymbol{\sigma} \cdot \mathbf{d}_3) dA, \tag{7}$$

where $\boldsymbol{\sigma}$ is the stress tensor and the integrals are taken over the cross section. N_1 and N_2 are the shear forces acting on the section in the $\mathbf{d}_1$ and $\mathbf{d}_2$ directions, respectively, and N_3 is the normal force. M_1 and M_2 are the moments associated with bending around the $\mathbf{d}_1$ and $\mathbf{d}_2$ directions, respectively, and M_3 is the moment associated with twisting. Conservation of linear momentum in the rope requires

$$\rho A \frac{D\mathbf{V}}{Dt} = \mathbf{N}' + \rho A \mathbf{g}, \tag{8}$$

where **g** is the gravitational acceleration. Conservation of angular momentum requires

$$0 = \mathbf{M}' + \mathbf{d}_3 \times \mathbf{N}. \tag{9}$$

In writing Equation 9, we omit the terms arising from angular acceleration and gravity, which are negligible when the rope is slender (Blount 2010, Ribe et al. 2006a).

The conservation equations (Equations 8 and 9) are valid for a rope with any rheology. To specialize them for the case of a Newtonian fluid with constant viscosity η, we require constitutive relations that link the dynamical variables N_3, M_1, M_2, and M_3 to the kinematical variables Δ, ω_1, ω_2, and ω_3. These can be derived rigorously using asymptotic expansions in powers of a small slenderness parameter $\epsilon \ll 1$ (Ribe et al. 2006a) and are

$$N_3 = 3\eta A \Delta, \tag{10a}$$

$$M_1 = 3\eta I \boldsymbol{\omega}' \cdot \mathbf{d}_1, \quad M_2 = 3\eta I \boldsymbol{\omega}' \cdot \mathbf{d}_2, \quad M_3 = 2\eta I \boldsymbol{\omega}' \cdot \mathbf{d}_3, \tag{10b}$$

where $\boldsymbol{\omega} = \omega_i \mathbf{d}_i$, η is the dynamic viscosity, and $I \equiv \pi a^4/4$ is the moment of inertia of the cross section. For a given rope geometry, Equations 1, 8, 9, and 10 are 12 coupled scalar equations for

the 12 variables V_i, ω_i, N_i, and M_i, of order 12 with respect to the spatial (arcwise) derivatives. Four of those orders are associated with bending around the $\mathbf{d}_1$ direction, four with bending around the $\mathbf{d}_2$ direction, two with stretching, and two with twisting. The spatial order of the system increases to 21 for general time-dependent problems in which the rope's geometry is unknown (Ribe et al. 2006a). The temporal evolution of the geometry is then governed by Equations 3 and 5.

3. STEADY COILING: THEORY VERSUS EXPERIMENT

The theory of Section 2 can be used in conjunction with simple tabletop laboratory experiments to understand the phenomenon of steady coiling. **Figure 3** shows a typical experimental setup in which fluid with density ρ, kinematic viscosity $\nu \equiv \eta/\rho$, and surface tension coefficient γ is ejected downward through a hole of diameter $d \equiv 2a_0$ at a constant volumetric rate $Q \equiv \pi a_0^2 U_0$, where U_0 is the ejection speed. The working fluid either is ejected forcibly from a syringe pump as in **Figure 3** (Cruickshank 1980; Cruickshank & Munson 1981; Habibi et al. 2006, 2010; Maleki et al. 2004; Ribe et al. 2006b) or falls freely from a hole at the bottom of a reservoir (Barnes & MacKenzie 1959, Barnes & Woodcock 1958, Griffiths & Turner 1988, Habibi et al. 2006, Mahadevan et al. 1998, Maleki et al. 2004, Ribe et al. 2006b). The fluid falls onto a plate on which it forms a helical coil of radius R that rotates with angular frequency Ω about a vertical axis. The effective fall height is the distance H from the hole down to the first point of contact of the free portion of the rope with the pile of fluid accumulated on the plate. The radius of the trailing portion of the rope (tail) decreases downward in general under the pull of gravity, and its (nearly

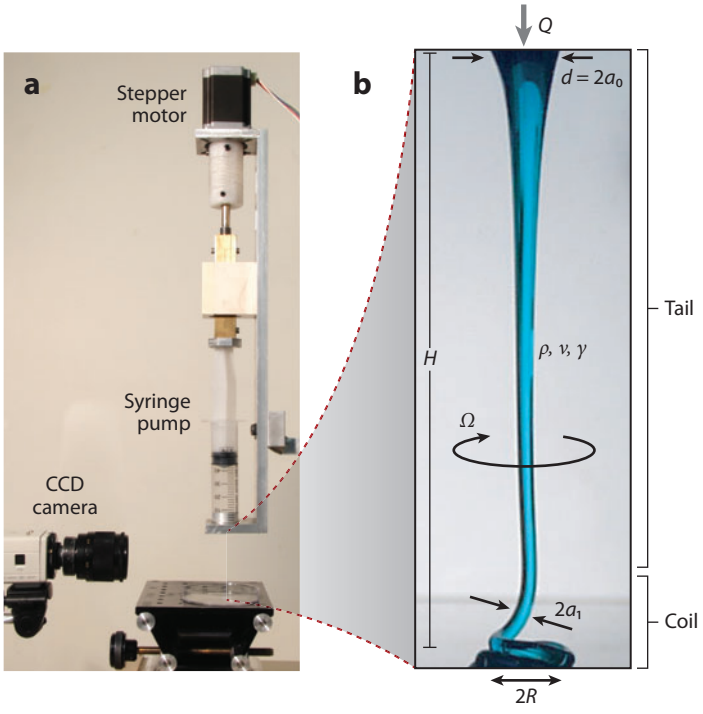

Figure 3

(*a*) Experimental setup for liquid rope coiling (IASBS, Zanjan). Figure taken from Ribe et al. (2008). (*b*) Parameters of liquid rope coiling. Figure modified from Ribe (2004).

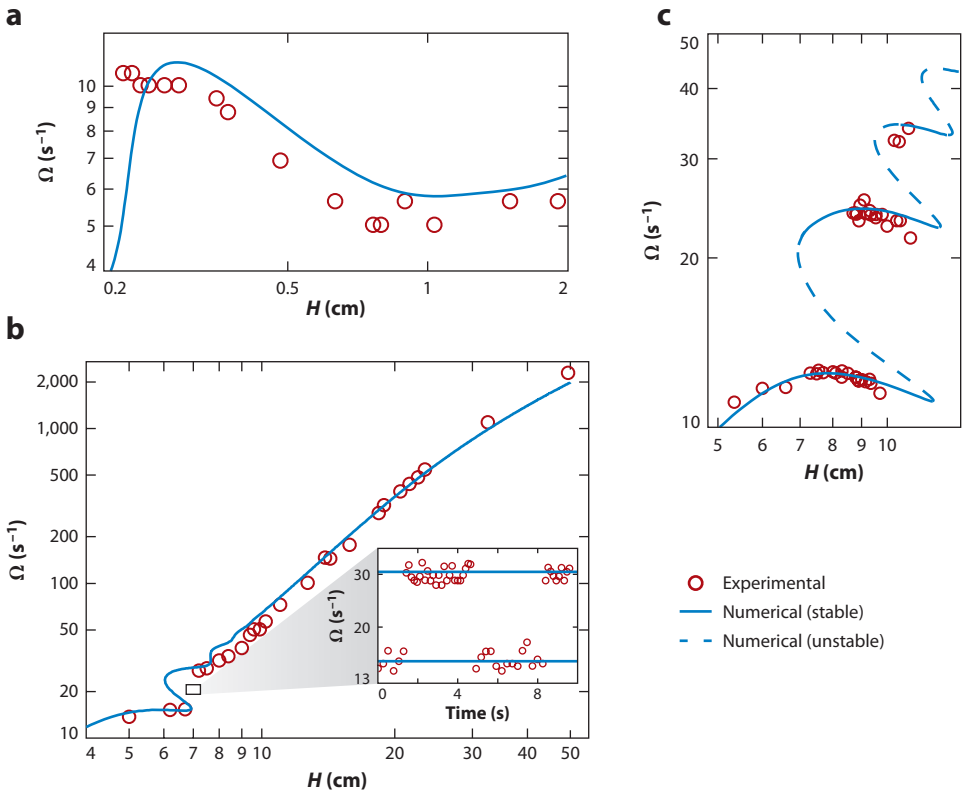

Figure 4

Comparison of experimental measurements (*red circles*) and numerical predictions (*blue lines*) of the angular frequency Ω of steady coiling as a function of the fall height H. The working fluid in the experiments is silicone oil with $\rho = 0.97$ g cm^{-3} and $\gamma = 21.5$ dyne cm^{-1}. (*a*) $d = 0.068$ cm, $Q = 0.0038$ ml s^{-1}, and $\nu = 10^5$ cSt. (*b*) $d = 0.5$ cm, $Q = 0.094$ ml s^{-1}, and $\nu = 3 \times 10^4$ cSt. The inset in panel *b* shows the coiling frequency as a function of time at $H = 7$ cm. (*c*) Same as in panel *a*, but with $Q = 0.00215$ ml s^{-1}. Steady coiling solutions along the dashed portions of the blue curve are unstable to small perturbations. Panels *a* and *b* taken from Maleki et al. (2004), and panel *c* taken from Ribe et al. (2006b).

constant) value in the coil is a_1. Finally, we note that $U_1 \equiv Q/\pi a_1^2$ is the axial velocity of the fluid at the contact point if the rope is in a steady-state configuration. Conservation of the mass flux through the moving contact point then requires $U_1 = R\Omega$.

Figure 4 shows experimental measurements of the coiling frequency Ω as a function of the fall height H for three different sets of values of d, ν, and Q (Maleki et al. 2004, Ribe et al. 2006b). The observed behavior is remarkably diverse. When H is small, Ω decreases as a function of H ($H < 1$ cm in **Figure 4*a***). If, however, H is a few tens of centimeters, Ω increases rapidly with H (**Figure 4*b***). For intermediate values of H, the curve $\Omega(H)$ has a gap for which a range of values of Ω is missing ($\Omega = 15$–30 s^{-1} in **Figure 4*b***). Closer examination shows that the gap corresponds to an oscillation between two coexisting coiling states with different frequencies (**Figure 4*b***, inset). The number of gaps is larger for larger values of ν and smaller values of Q. **Figure 4*c*** shows a case with three gaps, and up to four have been observed (Habibi et al. 2006).

The diversity of behavior in **Figure 4** can be understood with the help of a numerical model based on the theory of Section 2 (Ribe 2004). The model exploits the stationarity of coiling when observed from within the corotating reference frame. The dependent variables defined in Section 2 are then functions of the arc length s only and do not depend on time. Moreover, the acceleration term in the global force balance (Equation 8) becomes

$$\frac{D\mathbf{V}}{Dt} = U\,(U\mathbf{d}_3)' + 2\Omega U\mathbf{e}_3 \times \mathbf{d}_3 + \Omega^2\mathbf{e}_3 \times (\mathbf{e}_3 \times \mathbf{x}), \tag{11}$$

where $U(s) \equiv V_3(s)$ is the axial velocity of the fluid. The first term on the right-hand side of Equation 11 is the acceleration measured within the corotating frame, and the second and third terms are the Coriolis and centrifugal accelerations, respectively. The full system of equations reduces to a seventeenth-order geometrically nonlinear two-point boundary-value problem for a liquid rope of unknown shape, subject to appropriate boundary conditions at the ejection hole ($s = 0$) and at the rope's contact point with the fluid pile beneath the coil ($s = \ell$). Because both the frequency Ω and the rope length ℓ are unknown, 19 boundary conditions are required to close the problem. Solutions can be obtained numerically using a continuation method, whereby a simple analytical solution of the governing equations is gradually adjusted until it satisfies all the required boundary conditions (Ribe 2004).

The numerical predictions in **Figure 4** show the coiling frequency $\Omega(H)$ predicted by the numerical model for the same values of d, Q, and ν as in the corresponding laboratory experiment, and with the effect of surface tension included. The numerical predictions agree well with the observations without any adjustable parameters and successfully reproduce the diversity of behavior seen in the experiments. The comparison can be refined further by analyzing the stability of the numerical solutions to infinitesimal perturbations having the form of global modes (Ribe et al. 2006a). The unstable solutions are found at values of H for which the curve $\Omega(H)$ is multivalued and correspond closely to the gaps observed in the experiments (**Figure 4*c***).

Coriolis acceleration: the apparent acceleration $2\Omega \times \mathbf{V}$ of a body moving with velocity $\mathbf{V}$ in a noninertial reference frame rotating with angular velocity Ω

Centrifugal acceleration: the apparent acceleration $\Omega \times (\Omega \times \mathbf{x})$ of a body at a position $\mathbf{x}$ relative to the rotation axis in a noninertial reference frame rotating with angular velocity Ω

Continuation method: in the context of this review, a method for solving nonlinear boundary-value problems in which a simple analytical solution that satisfies modified forms of the equations and/or boundary conditions is gradually adjusted until it satisfies the true equations and boundary conditions

4. REGIMES OF STEADY COILING

The next issue is how to understand the physical mechanisms underlying the diversity of behavior in **Figure 4**. As a first step, we recalculate numerically the coiling frequency $\Omega(H)$ for the values of ν, d, and Q in **Figure 4*c***, but now over a much larger range of fall heights. The resulting curve (**Figure 5**) reveals that the different behaviors seen in **Figure 4** correspond to four distinct regimes of steady coiling, which appear in succession as the fall height increases. Each regime corresponds to a different balance among the viscous, gravitational, and inertial forces that control the motion of the rope.

The first regime, which we call viscous, corresponds to the decrease of the coiling frequency as a function of height for $0.03 < \hat{H} < 0.08$, where $\hat{H} \equiv H\,(g/\nu^2)^{1/3}$ is a dimensionless fall height. In this regime, the fall height is so small and coiling so slow that both gravity and inertia are negligible relative to viscous forces, which counterbalance each other in such a way that the net viscous force on each fluid element is zero. The viscous forces are primarily those that resist bending, which is the dominant mode of deformation everywhere. The rope in this regime therefore behaves like toothpaste squeezed from a tube onto a nearby surface, and its radius $\approx a_0$ is nearly constant (leftmost image in **Figure 5**).

In the viscous regime, the dynamical equations (Equations 8 and 9) reduce to $\mathbf{N}' = 0$ and $\mathbf{M}' + \mathbf{d}_3 \times \mathbf{N} = 0$. Because all the components of $\mathbf{N}$ and $\mathbf{M}$ are proportional to the viscosity η, the latter cancels out of the equations, so neither the radius R nor the frequency Ω of the coiling can depend on it. Furthermore, the rope radius a_0 ceases to be a relevant length scale in the limit

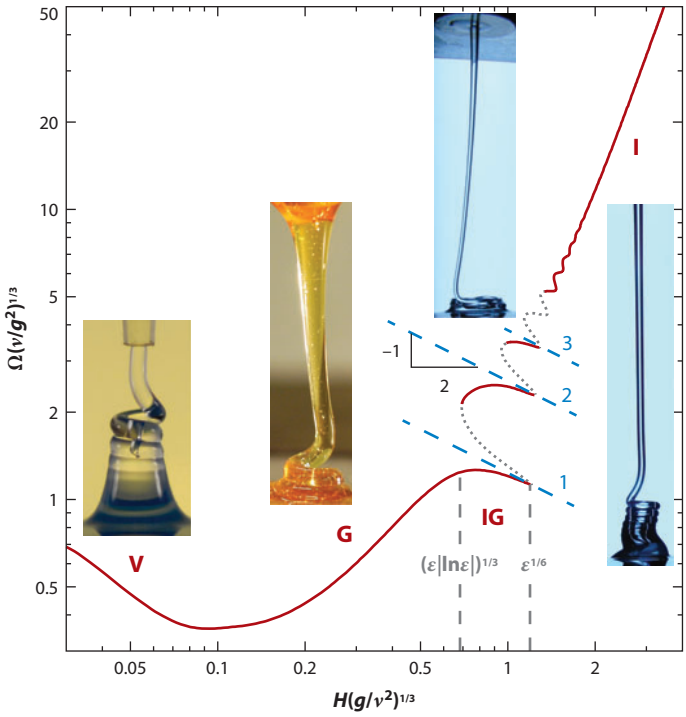

Figure 5

Four regimes of steady coiling, illustrated for the parameters of an experiment with silicone oil ($\rho = 0.97$ g cm^{-3}, $\nu = 10^5$ cSt, and $\gamma = 21.5$ dyne cm^{-1}) with $d = 0.068$ cm and $Q = 0.00215$ ml s^{-1} (Ribe et al. 2006b). The red curve shows the numerically predicted coiling frequency for these parameters, with its unstable portions dotted. The blue dashed lines indicate the first three eigenfrequencies (Equation 16) of a whirling viscous string that is strongly stretched by gravity. The parts of the curve corresponding to the viscous (V), gravitational (G), inertio-gravitational (IG), and inertial (I) regimes are labeled, and the typical appearance of the rope in each regime is shown. The transitional values of $H\,(g/\nu^2)^{1/3}$ separating the G, IG, and I regimes in the limit of a slender ($\epsilon \equiv a_1/H \ll 1$) rope strongly stretched by gravity are indicated at the bottom (Blount 2010, Ribe et al. 2006b). Figure modified from Ribe et al. (2008).

$a_0/H \ll 1$ corresponding to a very slender rope. The only parameters left are H and the injection speed U_0, and dimensional considerations then require (Ribe 2004)

$$R \sim H\,, \quad \Omega \sim \frac{U_0}{H} \quad \text{(viscous regime)}. \tag{12}$$

The above expression for Ω explains why the coiling frequency decreases with the fall height in the viscous regime. Even though R and Ω are independent of η and a_0, the force required to eject the fluid at the given speed U_0 will of course depend on both η and a_0.

The next regime in **Figure 5** is the gravitational regime, which occurs for $0.2 \le \hat{H} \le 0.6$. The coiling frequency now increases as a function of height, and the rope exhibits a clear bipartite (coil/tail) structure. Gravity balances viscous forces in both the coil (in which the deformation is dominated by bending) and the tail (dominated by stretching). In the coil, the viscous-gravity balance requires $M'' \sim \rho Ag$, where M denotes either of the bending moments M_1 or M_2. Now $M'' \sim M/\delta^2$, where δ is the arcwise extent of the portion of the rope in which bending stresses are important. Moreover, Equation 10b implies $M \sim \eta a_1^4 U_1/\delta^2 \sim \eta a_1^2 Q/\delta^2$, so $M'' \sim \rho Ag$ yields

(Ribe et al. 2006b)

$$\delta \sim \left(\frac{\nu Q}{g}\right)^{1/4}. \tag{13}$$

Catenary: the shape adopted by a string hanging in a field of gravity and supported at its two ends

However, δ is not the same as the coil radius R, for subtle reasons involving the nature of the interaction between the coil and the tail (Blount 2010). The tail behaves as a heavy catenary whose deflection from the vertical is maintained by a horizontal force exerted at its base by the bending stresses in the coil. Because inertia is negligible in the gravitational regime, that force is directed radially inward toward the coiling center to leading order. Moreover, because the deflection of a hanging catenary (solid or fluid) produced by a small horizontal force F is $O(F|\ln F|)$, a logarithmic term should be present in the expressions for R and Ω. This expectation is confirmed by a careful analysis using matched-asymptotic expansions (Blount 2010), which yields

$$R \sim \delta\left(\ln\frac{H}{\delta}\right)^{1/2}, \quad \Omega \sim \frac{U_1}{\delta}\left(\ln\frac{H}{\delta}\right)^{-1/2} \quad \text{(gravitational regime)}. \tag{14}$$

Because $H/\delta \approx 10$–150 for typical experimental situations, $\sqrt{\ln(H/\delta)} \approx 1.52$–$2.24$.

The third regime in **Figure 5** is a multivalued inertio-gravitational regime in the range $0.7 < \hat{H} < 1.4$, in which several different coiling frequencies are seen for a fixed value of the fall height. The complexities of this regime result from the effects of inertia, which influences the tail and the coil in different ways. Useful insight into the dynamics can be obtained by studying a simplified whirling viscous string model for the tail, in which gravity and the viscous forces that resist deformation by stretching are balanced by the centrifugal acceleration. The component of this force balance in the direction normal to the tail is (Ribe et al. 2006b)

$$\frac{gH}{k}\sin\frac{k(H-s)}{H}r'' - gr' + \Omega^2 r = 0, \tag{15}$$

where $r(s)$ is the horizontal radial deflection of the tail from the vertical, and k satisfies $2B\cos^2(k/2) = 3k^2$ with $B = gH^2/(\nu U_0)$. The first term in Equation 15 is the normal component of the axial viscous force $(N_3\mathbf{d}_3)'/(\rho A)$ per unit length of the tail and is nonzero because the tail's axis is curved. Its form takes into account the variation of the cross-sectional area $A(s)$ due to gravitational stretching of the tail. The limit $k = \pi$ ($B \to \infty$) corresponds to strong gravitational stretching, whereas $k = 0$ ($B \to 0$) corresponds to an unstretched tail with constant section A.

Equation 15 together with the relevant boundary conditions $r(0) = 0$ and $r(H)$ finite is a singular boundary/eigenvalue problem that has nontrivial solutions only for particular values Ω_n ($n = 1, 2, \ldots$) of the angular frequency Ω. Nondimensionalization of Equation 15 using the length scale H shows that these eigenvalues have the form

$$\Omega_n = C_n(B)\left(\frac{g}{H}\right)^{1/2}, \tag{16}$$

where $(g/H)^{1/2}$ is the angular frequency of a simple pendulum. For $B \neq 0$, the coefficients $C_n(B)$ must be determined numerically (Ribe et al. 2006b). The first three eigenvalues in the strong-stretching limit $B \to \infty$ are shown in **Figure 5**. They correspond closely to the locations of the downward-/rightward-facing peaks in the calculated coiling frequency curve $\Omega(H)$. This suggests that inertio-gravitational coiling is a resonance phenomenon in which the tail behaves as a weakly forced circular pendulum whose eigenmodes are excited when their frequencies are close to the frequency (Equation 14) imposed by the coil. The shape of the gravest ($n = 1$) eigenmode is shown by the image of inertio-gravitational coiling in **Figure 5**. Furthermore, the relations $\Omega \sim (g/H)^{1/2}$, $U_1 = R\Omega$, and $U_1 \sim gH^2/\nu$ (valid in the strong-stretching limit $B \gg 1$) imply that the amplitude of the tail's motion ($\approx R$) increases strongly ($\sim H^{5/2}$) as one approaches a peak in the $\Omega(H)$ curve from the left. Those peaks are therefore classic resonance peaks, whose amplitudes

are prevented from increasing without limit by the increasing importance of inertia in both the tail and the coil as the system approaches resonance (Blount 2010, Ribe et al. 2006b).

The last regime in **Figure 5** is an inertial regime that occurs for $\hat{H} > 1.8$. The tail in this regime is almost perfectly vertical (rightmost image in **Figure 5**). In the coil, the viscous forces that resist bending are balanced by inertia, implying $M'' \sim \rho a_1^2 \Omega^2 R$. The arcwise extent δ of the bending region is proportional to the coil radius R in this regime, so $M'' \sim \eta a_1^4 U_1 / R^4$, from which (Mahadevan et al. 2000)

$$R \sim \left(\frac{\nu a_1^4}{Q}\right)^{1/3}, \quad \Omega \sim \left(\frac{Q^4}{\nu a_1^{10}}\right)^{\frac{1}{3}} \quad \text{(inertial regime)}. \tag{17}$$

Finally, the relation between a_1 and H in the limit $B \gg 1$ depends on the value of $\hat{H}$. For $\hat{H} < 2$, the weight of the fluid in the tail is balanced primarily by the viscous resistance to stretching, and $a_1 \sim (\nu Q / g H^2)^{1/2}$. For $\hat{H} > 10$, the weight is balanced primarily by the vertical momentum flux, and $a_1 \sim (Q^2 / g H)^{1/4}$.

5. ONSET AND CESSATION OF COILING

Most of the coiling experiments described in Sections 3 and 4 were performed using very viscous silicone oil ($\nu = 3 \times 10^4$ or 10^5 cSt). Experiments with less viscous oils [$\nu = 330$–$2{,}220$ cSt (Habibi et al. 2010)] reveal striking new phenomena and help us better understand the conditions for the onset and cessation of the coiling instability.

The experiments in question show that three distinct states of the rope can exist for a given set of values of the experimental parameters ν, Q, and H. These are axisymmetric stagnation flow (**Figure 6*b***), steady coiling (**Figure 6*f***), and a novel rotatory folding state in which the rope folds back upon itself periodically while rotating about a vertical axis with a frequency equal to 3%–4% of the folding frequency (**Figure 6*a–d***). **Figure 7** shows the phase diagram of these states in the

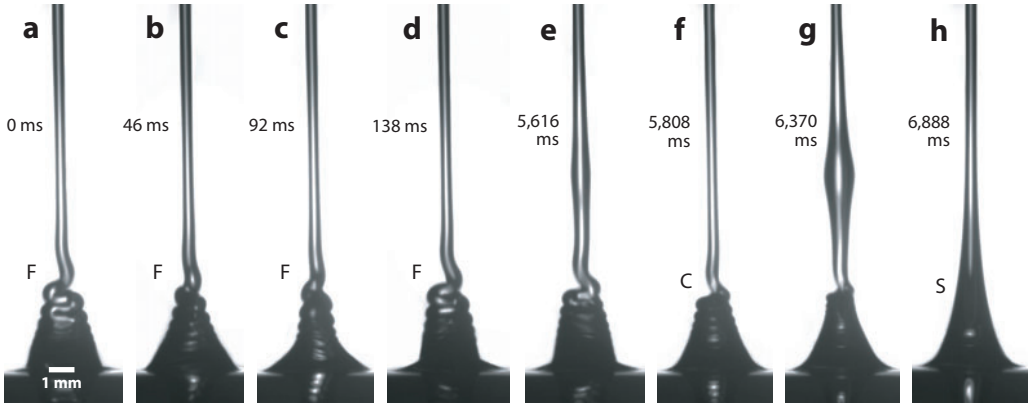

Figure 6

Time sequence of photographs showing three possible states of a liquid rope with $\nu = 950$ cSt, $Q = 0.19$ ml s^{-1}, $d = 2.6$ mm, and $H = 14$ cm: (*a–d*) folding with rotation (F), (*f*) steady coiling (C), and (*b*) axisymmetric stagnation flow (S). Panels *a–d* are separated by one-fourth of the rotation period of the folding plane. Panels *e* and *g* show the finite-amplitude perturbations that trigger the transitions between states. See Supplemental Video 1, in which each frame is 1 cm wide, and the playback rate is 1/20 real time (follow the Supplemental Material link from the Annual Reviews home page at **http://www.annualreviews.org**). Figure taken from Habibi et al. (2010).

Supplemental Material

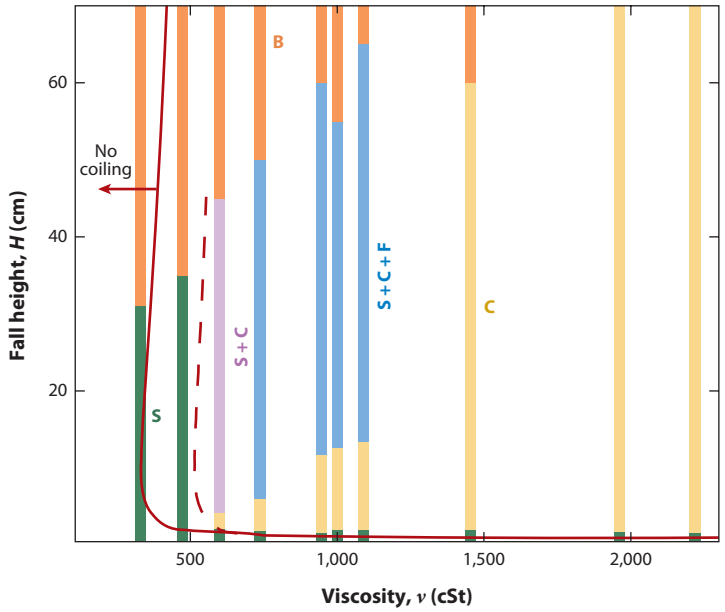

Figure 7

Phase diagram for steady stagnation flow (S), steady coiling (C), and rotatory folding (F) as functions of viscosity ν and fall height H for a fixed flow rate $Q = 0.131 \pm 0.006$ cm^3 s^{-1}. The orange (B) portions of the diagram correspond to episodic capillary breakup of the rope. The solid line (*red*) is the numerically calculated coiling cessation surface (including the effect of surface tension) separating regions in which coiling solutions exist (above/to the right) and do not exist (below/to the left). The dashed line shows the approximate location of the coiling cessation surface in the laboratory experiments. Figure taken from Habibi et al. (2010).

ν-H plane for a fixed flow rate $Q = 0.131$ cm^3 s^{-1}. In the B portion of the diagram, the rope breaks up episodically via capillary (Rayleigh-Plateau) instability. The S+C and S+C+F portions are multistable regions in which different states are observed at different times during a single experiment performed at fixed values of ν, Q, and H. The transitions between the states were triggered by finite-amplitude perturbations propagating down the rope, which were generated by tapping the experimental apparatus lightly (**Figure 6*e*,*g***).

In **Figure 7**, the onset of coiling corresponds to the boundary between the S region and the C or S+C region. For $\nu > 600$ cSt, the boundary is nearly horizontal so that coiling occurs when the fall height exceeds a critical value. For $\nu < 600$ cSt, however, the boundary becomes nearly vertical, and coiling occurs when the viscosity exceeds a critical value. More generally, the coiling/no-coiling boundary is a critical hypersurface in the (H, ν, Q, d) parameter space. One way to determine its shape is to analyze the stability of a steady axisymmetric stagnation flow to small perturbations (Tchavdarov et al. 1993), which yields the coiling onset surface in the (H, ν, Q, d) space. However, the only steady axisymmetric solution of the governing equations for a liquid rope falling onto an impermeable plate is one with infinite radius at the plate (Tchavdarov et al. 1993), which is not very realistic. An alternate procedure is to begin from a finite-amplitude coiling solution and then use a continuation procedure to locate the coiling cessation surface in the (H, ν, Q, d) space on which the solution ceases to exist (Habibi et al. 2010). Owing to hysteresis, the coiling cessation surface determined in this way need not coincide with the coiling onset surface.

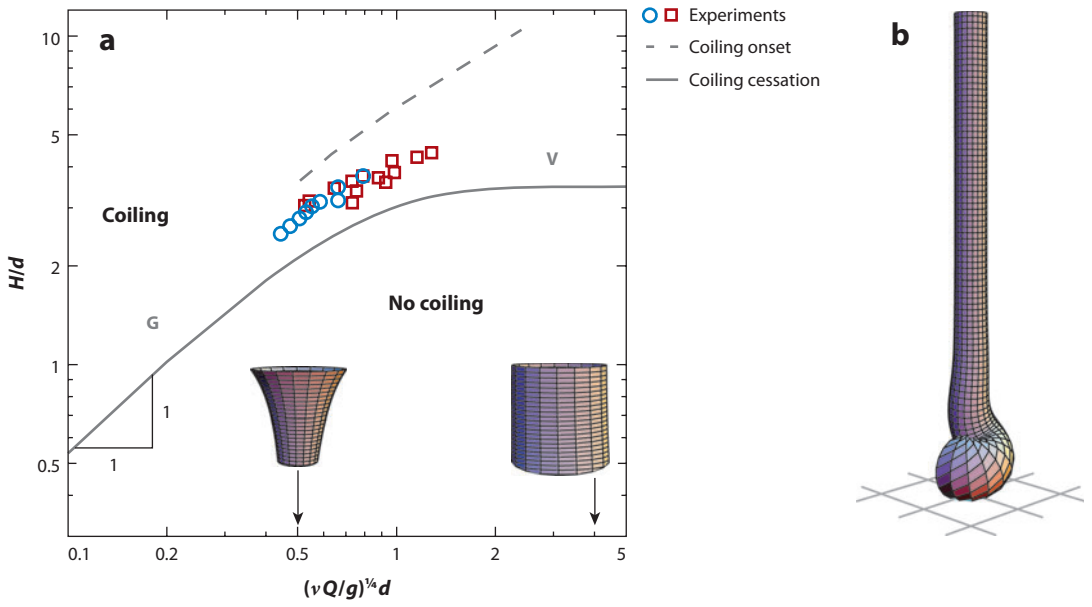

Figure 8

(*a*) Critical heights for the onset and cessation of steady coiling in the inertia-free limit. The solid line is the coiling cessation surface separating regions in which numerical steady coiling solutions without surface tension exist (above) and do not exist (below). The portions corresponding to the viscous (V) and gravitational (G) limits are indicated. The dashed line is the coiling onset surface in the absence of surface tension predicted by linear stability analysis (Tchavdarov et al. 1993). The colored symbols show experimentally measured critical heights (Cruickshank 1980) for silicone oil with $\gamma/\rho g d^2 = 0.0063$ (*blue circles*) and 0.014 (*red squares*). The inset images show the shapes of the uppermost part of the rope for $H/d = 4$ and for the values of $(\nu Q/gd^4)^{1/4}$ indicated by the arrows. (*b*) Numerically determined shape of the lower part of a liquid rope coiling in the inertial limit with the critical viscosity $\nu = \nu_I$, for $(\nu Q/gd^4)^{1/4} = 1.0$ and $H = 40(\nu^2/g)^{1/3}$ (Habibi et al. 2010). The width of each grid square on the bottom surface is $2(Q^2/gH)^{1/4}$. Figure taken from Habibi et al. (2010).

Neglecting surface tension for simplicity, one finds that the coiling cessation surface has three asymptotic limits corresponding to three distinct force balances: viscous, gravitational, and inertial. In both the viscous and gravitational limits, inertia is negligible. Coiling ceases when $H < F(\Pi)d$, where $\Pi = (\nu Q/gd^4)^{1/4}$ and $F(\Pi)$ is shown in **Figure 8*a***. In the viscous limit ($\Pi \gg 1$), gravity is negligible and the column diameter $\approx d$ everywhere. Coiling ceases when

$$H < 3.49d \equiv H_V. \tag{18}$$

In the gravitational limit ($\Pi \leq 0.5$), gravity strongly stretches the rope, so d is no longer a relevant length scale. Coiling ceases when

$$H < 5.4(\nu Q/g)^{1/4} \equiv H_G. \tag{19}$$

When H exceeds the critical values H_V or H_G, one recovers the viscous or gravitational regimes, respectively, of finite-amplitude coiling described in Section 4.

In the inertial limit, coiling ceases when

$$\nu < 0.665(gHQ^2)^{1/4} \equiv \nu_I. \tag{20}$$

The physical meaning of Equation 20 is that coiling can no longer occur when the radius R of the coil decreases so much that it becomes comparable with the radius a_1 of the rope itself. Let us consider a coiling rope with H sufficiently large that inertia is important in both the coil and

the tail. In the coil, inertia is balanced by viscous forces (the inertial regime of Section 4) so that $R \sim (\nu a_1^4/Q)^{1/3}$ (Mahadevan et al. 2000). In the tail, by contrast, inertia is balanced by gravity (free fall), implying $a_1 \sim (Q^2/gH)^{1/4}$. Therefore, R becomes comparable with a_1 when ν drops below a critical value $\nu_I \sim (gH\,Q^2)^{1/4}$, in agreement with Equation 20. This analysis is confirmed visually by the fact that $R \approx a_1$ in numerical solutions of steady coiling with $\nu = \nu_I$ (**Figure 8*b***).

The theoretically predicted coiling cessation surface can be compared with laboratory experiments in both the inertia-free (Cruickshank 1980) and inertial (Habibi et al. 2010) limits. **Figure 8*a*** shows critical heights measured in the viscous and gravitational limits with small values of the dimensionless surface tension parameter $\gamma/\rho g d^2$ (Cruickshank 1980). Also shown is the coiling onset surface predicted by a linear stability analysis in the absence of surface tension (Tchavdarov et al. 1993). The experimental measurements lie roughly midway between the coiling cessation and onset surfaces. To make a similar comparison in the inertial limit, one must first recalculate the coiling cessation surface including the effect of surface tension, which is not negligible in the experiments of Habibi et al. (2010). The cross section $Q = 0.131$ cm^3 s^{-1} of the resulting surface is shown in **Figure 7**. Its nearly horizontal portion ($\nu > 500$ cSt) corresponds to the gravitational limit, and its nearly vertical portion ($\nu < 500$ cSt) to the inertial limit. The theoretical coiling cessation surface successfully reproduces the overall trend of the observations, including the sharp transition between the critical-height ($\approx$ horizontal) and critical-viscosity ($\approx$ vertical) portions of the observed boundary between stagnation flow (S in **Figure 7**) and coiling (C and S+C in **Figure 7**). However, the theoretical coiling cessation surface is shifted too far to the left by approximately 40%. This is probably because the equations of Section 2 are less accurate when the slender-body assumption is violated locally, as it typically is for coiling near the coiling cessation surface (see **Figure 8*b***).

The results shown in **Figure 8** suggest an illuminating comparison between the buckling of viscous and elastic columns. Taylor (1969) noted that viscous and elastic buckling are analogous in that both require a compressive axial stress. However, the criteria for the onset of buckling in the two cases are quite different, a result that can be understood in terms of the following simple derivation. Let us consider the buckling of a cylindrical column of length H and constant diameter d in the limit of negligible gravity, inertia, and surface tension. We suppose further that the buckling is confined to the $\mathbf{d}_1$-$\mathbf{d}_3$ plane so that $\kappa_1 = \kappa_3 = M_1 = N_2 = 0$ by symmetry. We let $\zeta(s)$ be the lateral deflection of the axis of the column and its characteristic amplitude be ζ_0. In the absence of inertia and gravity, Equation 8 and 9 reduce to $N_1' = -\kappa_2 N_3$ and $M_2' = -N_1$, respectively. Combining these and noting that $\kappa_2 = \zeta''$ for small deflections, we obtain

$$M_2'' = \zeta'' N_3, \tag{21}$$

which is valid for both elastic and viscous columns. For an elastic column, $M_2 = EI\kappa_2$ (Love 1944), so the left-hand side of Equation 21 scales as $M_2'' \sim Ed^4\zeta_0/H^4$. The right-hand side scales as $\zeta'' N_3 \sim \zeta_0 d^2 P/H^2$, where P is the axial compressive stress. Balancing these two terms at the onset of buckling ($H = H_{\text{crit}}^{\text{elastic}}$), we obtain

$$H_{\text{crit}}^{\text{elastic}} \sim d\left(\frac{E}{P}\right)^{1/2}, \tag{22}$$

in agreement with the classic result of Euler (Landau & Lifshitz 1986, section 21). For a viscous column, by contrast, $M_2 = 3\eta I(V_1' + \kappa_2 V_3)'$ and $N_3 = 3\eta A V_3'$. Noting that $V_1 = \partial_t \zeta$ and using the scalings $V_3 \sim V_3^{\max}$ and $\partial_t \sim V_3^{\max}/H$, we find $M_3'' \sim \eta\zeta_0 d^4 V_3^{\max}/H^5$ and $\zeta'' N_3 \sim \eta\zeta_0 d^2 V_3^{\max}/H^3$. The balance of these two terms at the onset of buckling implies

$$H_{\text{crit}}^{\text{viscous}} \sim d, \tag{23}$$

in agreement with Equation 18. We note that the viscous buckling criterion (Equation 23), unlike the elastic criterion (Equation 22), is a purely geometrical one that depends on neither the material modulus (viscosity) nor the magnitude of the axial compressive stress. The reason is that both the bending moment M_2 and the force N_3 in a viscous column are proportional to the viscosity and to the applied stress. Both quantities therefore cancel out when the two terms in Equation 21 are balanced. In an elastic column, by contrast, M_2 does not depend on the applied stress while N_3 is independent of the material modulus, so both quantities appear in the torque balance (Equation 21). Yet despite its different onset criterion, finite-amplitude coiling of elastic ropes exhibits regimes that are analogous to those of viscous coiling, involving different balances of the elastic, gravitational, and inertial forces acting on the rope (Habibi et al. 2007).

6. NOVEL PHENOMENA AND NEW DIRECTIONS

In addition to steady coiling, liquid ropes falling onto surfaces can also exhibit a surprising range of time-dependent behavior. The phenomena we now describe have been discovered mostly within the past few years and are still imperfectly understood.

Figure 9*a* illustrates the generation of propagating spiral waves of air bubbles by liquid rope coiling (Habibi et al. 2008). Within limited ranges of values of ν, Q, and H near the boundary between the gravitational and inertio-gravitational regimes (Section 4), coiling is observed to be inherently unsteady such that the coiling center executes a slow retrograde precession whose frequency and radius are roughly 25% of those for the coiling itself. Consequently, each new coil of the liquid rope that is laid down is slightly displaced from the previous one, facilitating the trapping of small air bubbles between them. Moreover, because the precession and coiling

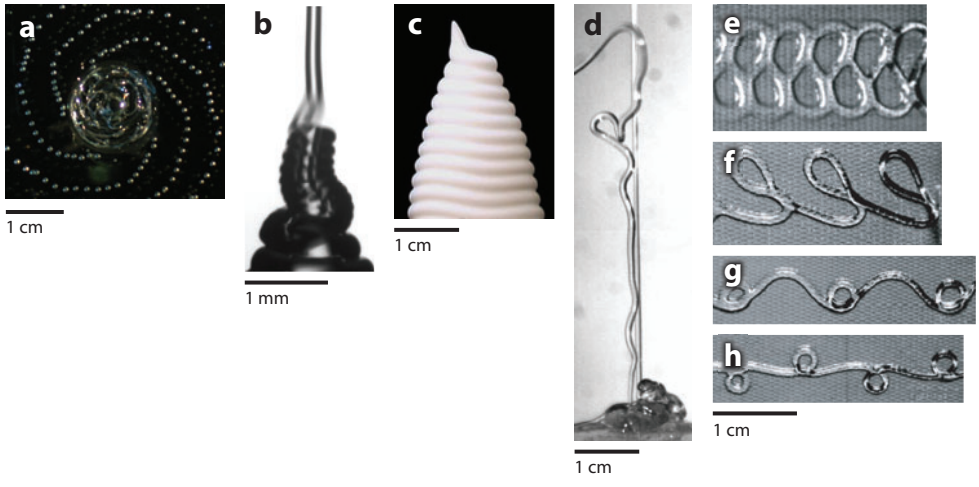

Figure 9

Nonstationary behaviors of falling liquid ropes. (*a*) Spiral waves of air bubbles generated by coiling with $d = 1.6$ mm, $\nu = 3 \times 10^4$ cSt, $Q = 0.137$ ml s^{-1}, and $H = 3.9$ cm. (*b*) Supercoiling of a liquid rope with $\nu = 2{,}200$ cSt, $Q = 0.315$ ml s^{-1}, and $H = 28$ cm. (*c*) Structure produced by steady coiling of a yield-stress fluid (shaving cream). (*d*) Kaye effect for a falling rope of commercial shampoo. Photograph courtesy of T. Majmudar. (*e–h*) Selected patterns formed by the fluid-mechanical sewing machine with the belt moving to the left. Panels *e–h* taken from Chiu-Webster & Lister (2006), reproduced with permission from Cambridge University Press.

frequencies are (apparently) incommensurable, the discrete azimuthal position where bubbles are trapped migrates continuously without ever returning to a previous value. Once trapped, a bubble is advected downward in the collapsing pile of coils and then radially outward in the thin layer of fluid spreading over the plate. The combination of the radial advection with the slow azimuthal drift of the trapping point gives rise to spiral waves of bubbles in the thin fluid layer (**Figure 9*a***).

A kinematic model for spiral bubble waves was proposed by Habibi et al. (2008) and predicts reasonably well the observed patterns given the measured values of the frequencies and radii for both the coiling and the precession. However, the underlying dynamical issues remain unsolved. Why does precession occur in the first place and with the frequency and radius it is observed to have? Why does it occur only near the limit between the gravitational and inertio-gravitational coiling regimes? And what is the precise mechanism by which air bubbles are trapped between successive coils?

A second surprising phenomenon is the supercoiling of a liquid rope (**Figure 9*b***). This occurs when the tall stack of coils formed by inertial coiling (**Figure 1*a***) itself becomes unstable to a secondary steady coiling instability with a frequency much lower than that of the primary one. However, supercoiling is not the only possible behavior of stacked coils in the inertial regime, which can also exhibit perfectly steady coiling (e.g., **Figure 6*f***) or periodic collapse (Habibi et al. 2006, figure 10). The phase diagram for these different behaviors has not been determined experimentally.

Additional new phenomena appear when the falling liquid rope has a non-Newtonian rheology. **Figure 9*c*** shows the slow coiling of a yield-stress fluid (shaving cream). Because no flow occurs when the stress in the rope is below the yield stress, a tall stack of coils that is stable against gravitational collapse can be generated even in the limit of negligible inertia. If, however, the rope has a shear-thinning rheology, it can exhibit an effect first documented by Kaye (1963) in which the falling stream occasionally leaps upward from the heap of fluid already deposited on the plate (**Figure 9*d***). Detailed experimental studies of this leaping-shampoo effect have been conducted by Collyer & Fischer (1976), Versluis et al. (2006), and Binder & Landig (2009). However, there is still no consensus on the physical mechanism involved. Versluis et al. (2006) suggested that a shear-thinning rheology alone is sufficient and that the fluid need not be elastic, whereas Binder & Landig (2009) stated that elasticity is necessary and that an air layer between the rope and the heap plays an important role. An air layer is present in the related phenomenon of a Newtonian rope rebounding from the free surface of a moving bath of the same fluid (Thrasher et al. 2007), which suggests that noncoalescence of the rope with its bulk liquid (Amarouchene et al. 2001) may be a requirement for the Kaye effect.

Our final example is the fluid-mechanical sewing machine in which a slender liquid rope falls onto a belt moving at constant velocity V in its own plane (Blount & Lister 2011, Chiu-Webster & Lister 2006, Morris et al. 2008, Ribe et al. 2006c). When V is sufficiently large, the rope has the form of a steady dragged catenary confined to a vertical plane. When V drops below a critical value, however, the steady catenary state becomes unstable to a meandering instability in which the rope leaves a sinusoidal trace on the belt. Further decrease of V causes additional bifurcations to more complex patterns (Chiu-Webster & Lister 2006, Morris et al. 2008), some of which are shown in **Figure 9*e–b***. Numerical and theoretical analyses of the bifurcation to meandering (Blount & Lister 2011, Ribe et al. 2006c) show that the onset frequency is nearly identical to the frequency of steady ($V = 0$) coiling for the same experimental parameters and reveal that the structures of the lowermost portion of the rope in the two cases are similar. However, the physical mechanisms responsible for the more complex patterns remain to be elucidated. As this and the previous examples in this section show, the simple configuration of a liquid rope falling onto a surface continues to reveal surprising new phenomena and to open up promising directions for future research.

Supercoiling: the secondary coiling of a slender object that is already coiled at a smaller scale (e.g., DNA strands or telephone cords)

Kaye effect: the upward- and/or sideways-directed rebound (leaping) of a falling rope of shear-thinning fluid (e.g., shampoo) impinging on a heap of the same fluid previously deposited on a surface

SUMMARY POINTS

1. The coiling of a liquid rope falling onto a surface is an example of a buckling instability, in which a slender object subject to an axial compressive stress becomes unstable to deformation by bending. In general, a coiling liquid rope comprises a long, quasi-vertical tail that deforms mainly by gravity-induced stretching and a helical coil that deforms primarily by bending. Because the differential equations governing bending are of higher order than those describing stretching, the coil can be thought of as a boundary layer in which the bending stresses permit the satisfaction of all the boundary conditions at the surface onto which the rope falls.
2. The principal forces involved in coiling are gravity, inertia, and the viscous forces that resist deformation of the rope by stretching, bending, and twisting. In a reference frame that rotates with the coil, the total inertial force is the sum of (minus) the momentum flux along the rope and the centrifugal and Coriolis forces associated with the rotating reference frame. For typical experimental fluids, surface tension has a relatively minor influence on coiling.
3. Finite-amplitude coiling can occur in four distinct regimes that succeed each other as the fall height H increases. In the viscous regime (e.g., toothpaste squeezed from a tube onto a nearby surface), both gravity and inertia are negligible everywhere in the rope. In the gravitational regime (e.g., honey falling from a spoon over a distance H of approximately a few centimeters), inertia is still negligible, and gravity balances the viscous forces associated with stretching (in the tail) and bending (in the coil). In the inertio-gravitational regime (e.g., honey with $H \approx 5$–8 cm), the centrifugal force becomes important in the tail, which behaves like a weakly forced distributed pendulum that resonates with the coil. In the inertial regime (e.g., honey with $H > 10$ cm), the bending stresses in coil are balanced primarily by inertia.
4. The initial coiling instability of a liquid rope subject to axial compression can occur in three distinct limits (viscous, gravitational, inertial) that merge smoothly into the corresponding finite-amplitude coiling regimes. The scaling law for the inertial limit reveals that low-viscosity fluids such as water do not coil because the radius of the coil would be smaller than that of the rope itself.
5. Coiling liquid ropes exhibit several types of multistable behavior. In the inertio-gravitational regime, two or more distinct coiling states with different frequencies can be observed at a single fall height, corresponding to the excitation of different eigenmodes of the tail. Low-viscosity ropes falling from a given height in the inertial regime can exhibit either steady stagnation flow, steady coiling, or periodic folding with rotation of the folding plane. Finally, the stack of coils formed by inertial coiling can exhibit steady-state behavior, periodic collapse, or supercoiling.
6. Whereas the steady coiling of Newtonian fluids is now reasonably well understood, the exploration of more complicated situations such as the fluid-mechanical sewing machine and ropes with non-Newtonian rheology has only begun.

DISCLOSURE STATEMENT

The authors are not aware of any biases that might be perceived as affecting the objectivity of this review.

ACKNOWLEDGMENTS

We thank S. Chiu-Webster, T. Cubaud, C. de Novion, E. Guyon, T. Majmudar, and Mars Inc. for providing images. While writing this article, N.M.R. was partially supported by INSU (SEDIT program) and ANR (grant PTECTO) in France. The Laboratoire de Physique Statistique of the Ecole Normale Supérieure is UMR8550 of the CNRS, associated with the Université Pierre et Marie Curie and the Université de Paris 7–Denis Diderot.

LITERATURE CITED

Amarouchene Y, Cristobal G, Kellay H. 2001. Noncoalescing drops. *Phys. Rev. Lett.* 87:206104

Arne W, Marheineke N, Meister A, Wegener R. 2010. Numerical analysis of Cosserat rod and string models for viscous jets in rotational spinning processes. *Math. Models Methods Appl. Sci.* 20:1941–65

Barnes G, MacKenzie R. 1959. Height of fall versus frequency in liquid rope-coil effect. *Am. J. Phys.* 27:112–15

Barnes G, Woodcock R. 1958. Liquid rope-coil effect. *Am. J. Phys.* 26:205–9

Binder JM, Landig AJ. 2009. The Kaye effect. *Eur. J. Phys.* 30:S115–32

Blount MJ. 2010. *Bending and buckling of a falling viscous thread*. PhD thesis. Univ. Cambridge

Blount MJ, Lister JR. 2011. The asymptotic structure of a slender dragged viscous thread. *J. Fluid Mech.* 674:489–521

Buckmaster JD, Nachman A, Ting L. 1975. The buckling and stretching of a viscida. *J. Fluid Mech.* 69:1–20

Chiu-Webster S, Lister JR. 2006. The fall of a viscous thread onto a moving surface: a 'fluid mechanical sewing machine.' *J. Fluid Mech.* 569:89–111

Collyer AA, Fischer PJ. 1976. The Kaye effect revisited. *Nature* 261:682–83

Cruickshank JO. 1980. *Viscous fluid buckling: a theoretical and experimental analysis with extensions to general fluid stability*. PhD thesis. Iowa State Univ.

Cruickshank JO, Munson BR. 1981. Viscous fluid buckling of plane and axisymmetric jets. *J. Fluid Mech.* 113:221–39

Eggers J, Dupont TF. 1994. Drop formation in a one-dimensional approximation of the Navier-Stokes equations. *J. Fluid Mech.* 262:205–21

Entov VM, Yarin AL. 1984. The dynamics of thin liquid jets in air. *J. Fluid Mech.* 140:91–111

Griffiths RW, Turner JS. 1988. Folding of viscous plumes impinging on a density or viscosity interface. *Geophys. J.* 95:397–419

Habibi M, Maleki M, Golestanian R, Ribe NM, Bonn D. 2006. Dynamics of liquid rope coiling. *Phys. Rev. E* 74:066306

Habibi M, Møller PCF, Ribe NM, Bonn D. 2008. Spontaneous generation of spiral waves by a hydrodynamic instability. *Europhys. Lett.* 81:38004

Habibi M, Rahmani Y, Bonn D, Ribe NM. 2010. Buckling of liquid columns. *Phys. Rev. Lett.* 104:074301

Habibi M, Ribe NM, Bonn D. 2007. Coiling of elastic ropes. *Phys. Rev. Lett.* 99:154302

Kaye A. 1963. A bouncing liquid stream. *Nature* 197:1001–2

Landau LD, Lifshitz EM. 1986. *Theory of Elasticity*. New York: Pergamon. 3rd ed.

Love AEH. 1944. *A Treatise on the Mathematical Theory of Elasticity*. New York: Dover

Mahadevan L, Ryu WS, Samuel ADT. 1998. Fluid 'rope trick' investigated. *Nature* 392:140

Mahadevan L, Ryu WS, Samuel ADT. 2000. Correction: Fluid 'rope trick' investigated. *Nature* 403:502

Maleki M, Habibi M, Golestanian R, Ribe NM, Bonn D. 2004. Liquid rope coiling on a solid surface. *Phys. Rev. Lett.* 93:214502

Morris S, Dawes JHP, Ribe NM, Lister JR. 2008. Meandering instability of a viscous thread. *Phys. Rev. E* 77:066218

Ribe NM. 2004. Coiling of viscous jets. *Proc. R. Soc. Lond. A* 460:3223–39

Ribe NM, Habibi M, Bonn D. 2006a. Stability of liquid rope coiling. *Phys. Fluids* 18:084102

Ribe NM, Habibi M, Bonn D, Stutzmann E. 2008. Instabilités de flambage dans les fluides visqueux: Du laboratoire au manteau terrestre. *Reflets Phys.* 11:9–12

Ribe NM, Huppert HE, Hallworth MA, Habibi M, Bonn D. 2006b. Multiple coexisting states of liquid rope coiling. *J. Fluid Mech.* 555:275–97

Ribe NM, Lister JR, Chiu-Webster S. 2006c. Stability of a dragged viscous thread: onset of 'stitching' in a fluid mechanical 'sewing machine.' *Phys. Fluids* 18:124105

Taylor GI. 1969. Instability of jets, threads and sheets of viscous fluid. *Proc. 12th Int. Congr. Appl. Mech.*, ed. M Hetenyi, WG Vincenti, pp. 382–88. New York: Springer

Tchavdarov B, Yarin AL, Radev S. 1993. Buckling of thin liquid jets. *J. Fluid Mech.* 253:593–615

Thrasher M, Jung SW, Pang YK, Chuu CP, Swinney HL. 2007. The bouncing jet: a Newtonian liquid rebounding off a free surface. *Phys. Rev. E* 76:056319

Versluis M, Blom C, van der Meer D, van der Weele K, Lohse D. 2006. Leaping shampoo and the stable Kaye effect. *J. Stat. Mech.* 2006:P07007

Whittaker ET. 1944. *A Treatise on the Analytical Dynamics of Particles and Rigid Bodies*. New York: Dover. 4th ed.

Yarin AL. 1993. *Free Liquid Jets and Films: Hydrodynamics and Rheology*. New York: Longman

RELATED RESOURCES

Video of liquid rope coiling in the inertial regime: **http://www.youtube.com/watch?v=rEkuhC9eJlM&feature=related**

Video of folding instabilities in microchannels (T. Cubaud): **http://pof.aip.org/gallery_of_fluid_motion/2006_gallery/03_09_10_folding_of_viscous_threads_in_microfluidics**

Video of a periodic folding instability in the manufacture of dessert cakes (Unilever): **http://www.unilever.com/mediacentre/multimedia/foods/Vienetta.aspx**

Video of periodic folding of a falling lava stream (U.S. Geological Survey): **http://hvo.wr.usgs.gov/kilauea/update/archive/2009/Jun/RGbreakout_01Oct2009.mov**

Video of the Kaye effect (M. Versluis et al.): **http://www.youtube.com/watch?v=GX4_3cV_3Mw&feature=related**

Video of the fluid-mechanical sewing machine (S. Morris): **http://www.youtube.com/watch?v=CMYISqxS3K4**

Annual Review of
Fluid Mechanics

Volume 44, 2012

Contents

Indexes

Errata

An online log of corrections to *Annual Review of Fluid Mechanics* articles may be found at http://fluid.annualreviews.org/errata.shtml